Optics Letters

Circular dichroism in achiral metasurfaces induced by spatially selective coupling with molecules

Baojuan Han,[1] Xiaodong Yang,[1,3] and Jie Gao[2,*]

[1]Department of Mechanical and Aerospace Engineering, Missouri University of Science and Technology, Rolla, Missouri 65409, USA
[2]Department of Mechanical Engineering, Stony Brook University, Stony Brook, New York 11794, USA
[3]yangxia@mst.edu
*jie.gao.5@stonybrook.edu

Received 29 July 2024; revised 23 November 2024; accepted 9 December 2024; posted 9 December 2024; published 8 January 2025

Achiral metasurfaces with near-field optical chirality have attracted great attention in molecular sensing and chiral emission control. Here, the circular dichroism (CD) response of an achiral metasurface induced by spatially selective coupling with polymethyl methacrylate (PMMA) molecules is demonstrated. A designed achiral metasurface with a V-shaped resonator exhibits large optical chirality with a strongly dissymmetric distribution under circular polarization. By introducing a PMMA molecule layer on top of the metasurface, which covers the area with large optical chirality, CD in absorption of 0.38 and a dissymmetric factor of optical chirality g_c of 0.16 are obtained. Furthermore, an analysis of the coupled harmonic oscillator model reveals stronger coupling strength between the PMMA layer and the metasurface under RCP incidence, compared to the LCP case. Moreover, it is shown that the far-field CD response of the metasurface is linearly correlated with the dissymmetric near-field optical chirality distribution. The demonstrated results present the potential for advancing applications in chiral molecule vibrational sensing, thermal emission control, and infrared chiral imaging. © 2025 Optica Publishing Group. All rights, including for text and data mining (TDM), Artificial Intelligence (AI) training, and similar technologies, are reserved.

https://doi.org/10.1364/OL.537725

Circular dichroism spectroscopy is conventionally utilized to analyze chiral materials, which is of great significance in biomedical research and pharmaceutical industry. Chiral molecules are widespread in nature, which present structures not superimposable upon their mirror images [1]. Chiral materials are widespread in nature; however, due to the scale mismatch between molecule size and light wavelength, CD response is usually very weak. Chiral metasurfaces have been extensively explored to generate strong superchiral near-fields, which can enhance chiral light–matter interaction and thus provide effective detection of enantiomers with enhanced CD signals [2–4]. It has been discovered that the superchiral near-fields in chiral metasurface play a more important role in chiral molecule sensing, even for a chiral metasurface with low far-field CD [5].

Alternatively, achiral metasurface with mirror symmetry also possesses near-field optical chirality, and it can offer background-free chiral molecule sensing in contrast to chiral metasurface [6,7]. Different achiral metasurfaces have been developed to enhance local optical chirality and amplify molecular CD signals [6–9]. Furthermore, circularly polarized emission from a chiral radiative local density of states hot-spot in achiral metasurface has been applied to chiral photoluminescence, helicity-dependent binary encoding, and two-dimensional display applications [10,11]. However, the chiroptical response in an achiral metasurface by exploiting the strongly dissymmetric optical chirality distribution under circular polarization has not been extensively studied yet, especially for the application in mid-infrared vibrational molecular sensing.

In this work, the circular dichroism response of an achiral metasurface induced by spatially selective coupling with PMMA molecules is demonstrated. The designed achiral metasurface with a V-shaped resonator exhibits large optical chirality with a strongly dissymmetric distribution under circular polarization. By introducing a PMMA molecule layer on top of a metasurface, which covers the area with large optical chirality, CD in absorption of 0.38 is achieved due to the spatially selective coupling of PMMA molecules with the metasurface. Furthermore, the difference in the optical chirality distribution of the metasurface coupled with PMMA molecules under LCP and RCP incidences are examined, and a dissymmetric factor of optical chirality g_c of 0.16 is obtained. Moreover, the absorption spectra of the metasurface coupled with the PMMA molecules under LCP and RCP incidences are analyzed with the coupled harmonic oscillator model. It is shown that the coupling strength between the PMMA layer and the metasurface under a RCP incidence is stronger than that under a LCP incidence. It is also demonstrated that the far-field CD response of the metasurface is linearly correlated with the dissymmetric near-field optical chirality distribution. These results will provide new opportunities for advancing applications in chiral molecule vibrational sensing, spatially resolved molecular detection, thermal emission control, and infrared chiral imaging.

Figure 1(a) illustrates the schematic of the designed achiral metasurface on a three-layer gold–alumina–gold (Au–Al_2O_3–Au) structure, consisting of the V-shaped resonator in the top 65-nm-thick Au layer, the middle 250-nm-thick Al_2O_3 spacer layer, and the bottom 200-nm-thick Au mirror. The periods of the unit cell are $px = 5162$ nm and $py = 2547$ nm, respectively. The V-shaped resonator contains a horizontal slot with a length of $l_1 = 2559$ nm and a width of $w_1 = 910$ nm,

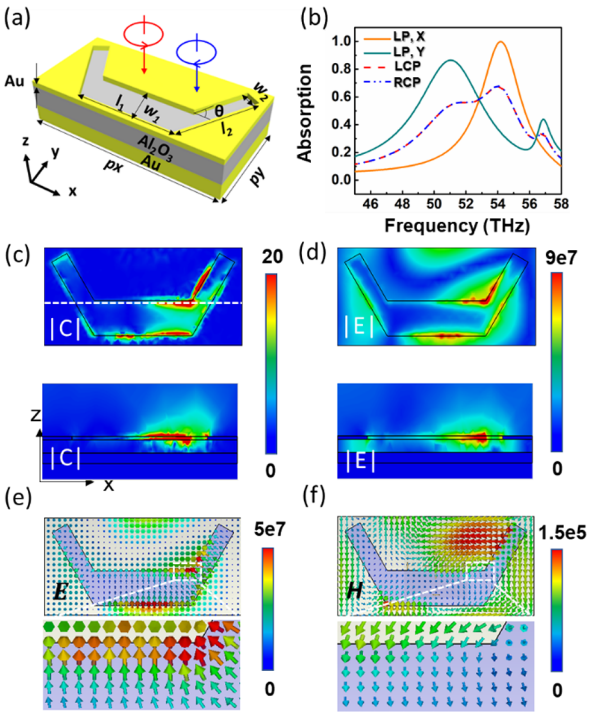

Fig. 1. (a) Schematic of the achiral metasurface unit cell. (b) Absorption spectra of the metasurface under LCP and RCP incidences (red and blue dashed curves), as well as under linearly polarized light (orange and green solid curves). (c), (d) Top and side views of optical chirality $|C|$ and electric field $|E|$ distributions of the resonance mode under RCP incidence at 52.5 THz. The top views are attained at the Au–Al_2O_3 interface, and the side views are along the white dashed line in (c). (e), (f) Distributions of vector fields $\boldsymbol{E}$ and $\boldsymbol{H}$ at the resonance, and the zoom-in views around the areas indicated by the white dashed boxes.

and two tilted slots with a length of $l_2 = 2210$ nm, a width of $w_2 = 455$ nm, and a rotation angle of $\theta = 60°$ relative to the horizontal slot. The optical responses of the achiral metasurface are simulated using the CST Studio Suite software. The Al_2O_3 permittivity is taken from experimental data [12], and the Au permittivity is described by the Drude model $\varepsilon_{\mathrm{Au}} = \varepsilon_\infty - \omega_p^2/(\omega^2 + i\gamma_p\omega)$, with the background dielectric constant $\varepsilon_\infty = 1$, the plasmon frequency $\omega_p = 1.37 \times 10^{16}$ rad/s, and the damping constant $\gamma_p = 12.24 \times 10^{13}$ rad/s for the Au thin film, which is three times that of the value for bulk gold [13,14]. Figure 1(b) presents the absorption spectra of the achiral metasurface under LCP and RCP light in dashed curves, where a broad plasmonic resonance of around 52.5 THz is featured. The LCP and RCP absorption spectra overlap with each other and there is no chiroptical response due to the structure symmetry. The solid curves show the plasmonic resonances excited by two orthogonal linear polarizations at 54 THz under x-polarized light and 51 THz under y-polarized light, respectively. The optical chirality for characterizing the chiral properties of the electromagnetic field is defined as $C = -\frac{\omega}{2c^2} Im(\boldsymbol{E}^* \cdot \boldsymbol{H})$[15–17], where $\boldsymbol{E}$ and $\boldsymbol{H}$ represent complex electric and magnetic fields. For circularly polarized light in free space, optical chirality C_0 is ±1 for RCP or LCP light when considering normalized units. Figure 1(c) shows the optical chirality distribution of the resonance mode under RCP incidence in the top and side views at 52.5 THz. A strongly dissymmetric distribution of optical

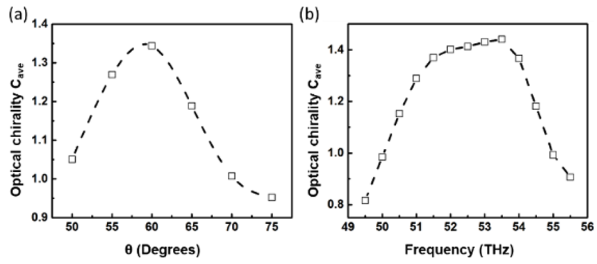

Fig. 2. Averaged optical chirality C_{ave} as a function of (a) the rotation angle θ and (b) the frequency.

chirality is observed in the metasurface, where the optical chirality is mostly confined at the slot edges in the right corner of the V-shaped resonator under RCP light, with a maximum value of around 20. The corresponding electric field distributions in Fig. 1(d) also show a strong confinement at the slot edges in the right corner. The side views in Fig. 1(c) and 1(d) indicate that the optical chirality and electric field are strongly confined around both the top and bottom surfaces of the V-shaped structure in the top Au layer. It is noteworthy that the optical chirality and electric field distributions under LCP incidence are the mirror images of those under RCP incidence due to the geometric symmetry of the V-shaped structure. Figures 1(e) and 1(f) present the vector field distributions of $\boldsymbol{E}$ and $\boldsymbol{H}$, respectively, where $\boldsymbol{E}$ and $\boldsymbol{H}$ have parallel components, which leads to large C values around the right corner of the resonator. It is noted that distinguished from many other achiral structures, the designed V-shaped achiral metasurface possesses a strongly dissymmetric distribution of optical chirality on either the left or right side of the structure depending on the incident circular polarization, which enables the spatially selective coupling between molecules and metasurface.

Among the geometric parameters of the V-shaped resonator, the rotation angle θ is critical for obtaining large optical chirality of the resonance mode. The averaged optical chirality C_{ave} over the volume V occupied by the metasurface resonance mode is defined by $C_{\mathrm{ave}} = \int |C| dV / \int |C_0| dV$, where C_0 is the optical chirality of incident circularly polarized light. Figure 2(a) depicts the averaged optical chirality C_{ave} as a function of the rotation angle θ. It shows that C_{ave} reaches the maximum value at around $\theta = 60°$ due to the large parallel components of the $\boldsymbol{E}$ and $\boldsymbol{H}$ fields. The maximum C_{ave} obtained at the optimized rotation angle suggests that the designed metasurface structure possesses strong superchiral near-fields located at the right side of the structure under RCP incidence as shown in Fig. 1(c). Figure 2(b) shows that the spectrum of C_{ave} has a similar profile as the circularly polarized absorption spectra in Fig. 1(b), and large C_{ave} values are maintained across the frequency range of the broad plasmonic resonance.

To introduce the chiroptical response of the metasurface for molecular sensing, an 80-nm-thick PMMA molecule layer is coated on top of the right side of a metasurface unit cell, which covers the area with large optical chirality of the V-shaped resonator, as shown in Fig. 3(a). Due to the coating of PMMA molecules, the plasmonic resonance of the metasurface shifts from 52.5 THz to 52 THz, which matches the infrared vibrational absorption of the C = O bond in the PMMA molecules [18]. The permittivity of the PMMA layer can be modeled as a Lorentz oscillator with $\varepsilon_{\mathrm{PMMA}} = \varepsilon_b - \frac{\varepsilon_L \omega_0^2}{\omega^2 + i\delta_0\omega - \omega_0^2}$, where the background permittivity is $\varepsilon_b = 2.2$, the Lorentz resonance

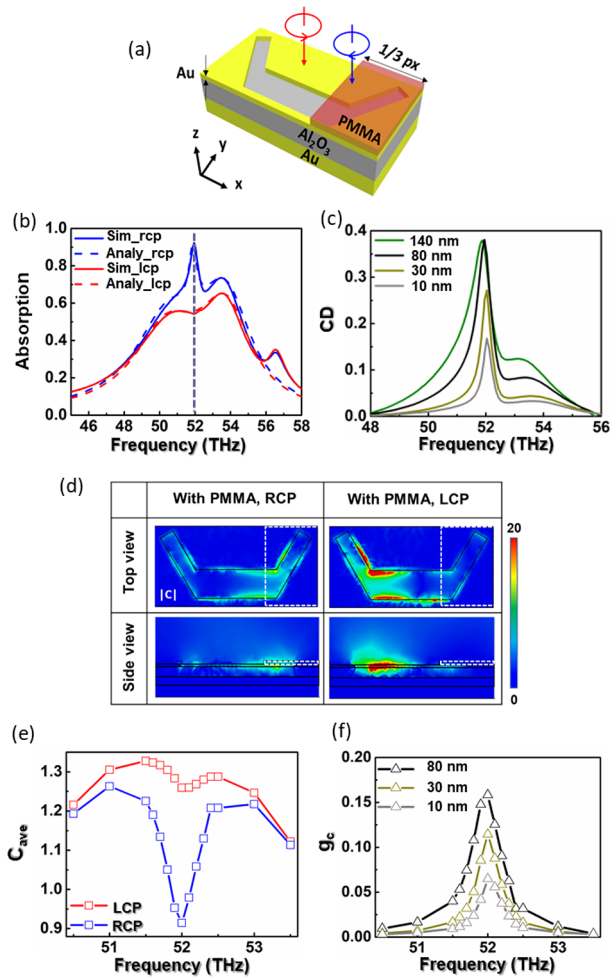

Fig. 3. (a) Schematic of the metasurface unit cell coated with the PMMA layer with a width of 1/3 *px*. (b) Simulated (solid lines) and calculated (dashed lines) absorption spectra of the metasurface with the 80-nm-thick PMMA layer under LCP and RCP illumination. (c) CD spectra of the metasurface with different PMMA thicknesses. (d) Top and side views of optical chirality distribution under RCP and LCP incidences for the metasurface coupled with the PMMA layer. The white dashed boxes indicate the PMMA molecule location. (e) C_{ave} as a function of frequency for LCP and RCP incidences. (f) g_c spectra of the metasurface with different PMMA thicknesses. The symbols represent simulated data points.

frequency is $\omega_0 = 3.269 \times 10^{14}$ rad/s, the Lorentz permittivity is $\varepsilon_L = 0.018$, and the Lorentz damping rate is $\delta_0 = 1.6 \times 10^{12}$ rad/s [12,19].

Figure 3(b) shows the simulated absorption spectra of the metasurface with a selectively coated PMMA layer under LCP and RCP incidences in solid curves. A sharp peak around 52 THz due to PMMA vibrational absorption is observed in the RCP absorption spectrum, while the LCP absorption spectrum is almost the same as that of the bare metasurface in Fig. 1(b). This is the result of spatially selective coupling of PMMA molecules with the metasurface under circularly polarized light, which is associated with the dissymmetric distribution of optical chirality with RCP and LCP incidences. The CD in absorption is defined as $\mathrm{CD} = A_{\mathrm{RCP}} - A_{\mathrm{LCP}}$, and the CD value of the metasurface induced by the 80-nm-thick PMMA layer is 0.38. It is worth noting that the selective coverage of the molecule layer on one side of the achiral metasurface breaks the mirror symmetry of the structure, while the spatially selective coupling between the molecule infrared vibrational mode and the metasurface resonance mode leads to the CD response. Figure 3(c) plots the CD spectra of the metasurface with PMMA thicknesses of 10 nm, 30 nm, 80 nm, and 140 nm. It shows that the peak CD value increases as the PMMA layer gets thicker due to the larger overlapped volume and the stronger coupling between the superchiral resonant field and the molecules. It is noted that there is no further CD increase for a PMMA layer thickness of more than 80 nm, as the electromagnetic field of the plasmonic resonance mode decays exponentially along the z direction above the top Au surface. Figure 3(d) shows the optical chirality $|C|$ distribution of the metasurface coupled with PMMA molecules. The optical chirality under RCP incidence in Fig. 3(d) becomes weaker than that of the bare metasurface in Fig. 1(c), indicating a strong coupling strength of the PMMA molecules with the metasurface resonance mode. On the other hand, the optical chirality under LCP incidence remains the same as that of the bare metasurface, as there is only a small spatial overlap between the PMMA layer and the optical chirality distribution of the resonance mode. The averaged optical chirality C_{ave} is further calculated and plotted in Fig. 3(e) to quantitatively illustrate the difference in optical chirality under LCP and RCP incidences. At a resonance frequency of 52 THz, C_{ave} under LCP incidence is 1.26, while it drops to 0.92 under RCP incidence. The dissymmetric factor of optical chirality is introduced as $g_c = (C_{\mathrm{ave,\,L}} - C_{ave,\,R})/C_{\mathrm{ave,\,L}} + C_{ave,\,R})$ to describe the difference of the averaged optical chirality $C_{\mathrm{ave,L}}$ and $C_{\mathrm{ave,R}}$ under LCP and RCP incidences. Figure 3(f) shows the g_c spectra of the metasurface with different PMMA thicknesses, where resonance peaks are observed at the frequency of 52 THz. It is shown that the g_c value for the 80-nm-thick PMMA layer is 0.16, and the value increases with the PMMA thickness in a similar trend as the CD spectra in Fig. 3(c).

The coupled harmonic oscillator model [20] is used to study the coupling strength between the PMMA molecules and the metasurface under LCP and RCP incidences. The y-polarized and x-polarized modes can be represented as two oscillators in the model with resonance frequencies of ω_1, ω_2 and damping rates of γ_1, γ_2, respectively. Under circular polarization illumination, the y-polarized and x-polarized modes are excited with externally applied harmonic driving forces $f_y e^{i\omega t \pm \pi/2}$ and $f_x e^{i\omega t}$, respectively. The positive (negative) sign in $f_y e^{i\omega t \pm \pi/2}$ represents the case of RCP (LCP) incidence. The coupling coefficient between the two modes is σ_{12}. Taking the absorption of the PMMA molecules into account, another harmonic oscillator with a resonance frequency of ω_3 and a damping rate of γ_3 is introduced to form a coupled system with three harmonic oscillators. The coupling coefficient between the PMMA molecules and the y-polarized (x-polarized) mode is $\sigma_{13}(\sigma_{23})$. The motion equations of the three harmonic oscillators are written as follows:

$$\begin{aligned} &\ddot{x_1} + \gamma_1\dot{x_1} + \omega_1^2 x_1 - \sigma_{12}x_2 - \sigma_{13}x_3 = f_y e^{i\omega t \pm \pi/2}, \\ &\ddot{x_2} + \gamma_2\dot{x_2} + \omega_2^2 x_2 - \sigma_{12}x_1 - \sigma_{23}x_3 = f_x e^{i\omega t}, \text{ and} \\ &\ddot{x_3} + \gamma_3\dot{x_3} + \omega_3^2 x_3 - \sigma_{13}x_1 - \sigma_{23}x_2 = 0. \end{aligned} \quad (1)$$

The displacements x_1, x_2, and x_3 of the oscillators are harmonic with $x_{1,2,3} = c_{1,2,3}e^{i\omega t}$, where the amplitude $c_{1,2,3}$ can be calculated analytically. The absorption spectrum is obtained by summing the square of the three oscillators' amplitudes. The analytical curves based on the model are depicted as the dashed lines in Fig. 3(b), which are in excellent agreement with the simulated curves. The fitting parameters used in the model are presented

Table 1. Parameters for the Coupled Harmonic Oscillator Model

	Bare Metasurface	With PMMA, RCP	With PMMA, LCP
ω_1 (THz), γ_1 (THz)	51.2, 4.67	50.8, 4.67	50.8, 4.67
ω_2 (THz), γ_2 (THz)	54.0, 3.457	53.5, 3.457	53.5, 3.457
ω_3 (THz), γ_3 (THz)	0, 0	51.9, 0.5	51.9, 0.5
σ_{12} (THz^2)	94.09 (RCP) -94.09 (LCP)	100	-106.09
σ_{13} (THz^2)	0	1.21	-0.01
σ_{23} (THz^2)	0	23.04	-0.01

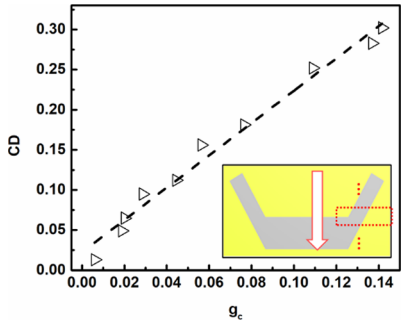

Fig. 4. Values of CD and g_c at each PMMA patch location (triangle symbols) and the linear fitting (dashed line). Inset shows the spatial displacement of the PMMA patch along the y direction, where the red dashed box indicates the location where the highest values of CD and g_c are obtained.

in Table 1. It is noted that the σ_{13} and σ_{23} values under RCP incidence are much higher compared to those under LCP incidence, suggesting stronger coupling strength between the PMMA layer and the metasurface under RCP incidence.

To further investigate the relationship between the values of CD and g_c under different spatially selective coupling conditions, a PMMA patch with the size of 1/3 px by 1/5 py is moved from top to bottom of the metasurface unit cell in the y direction in a step size of 200 nm, as illustrated in the inset of Fig. 4. By changing the spatial displacement of the PMMA patch, the coupling strength between the PMMA molecules and the metasurface resonance mode varies, which results in different chiroptical responses. The values of CD calculated from the absorption spectra and g_c obtained from the averaged optical chirality are displayed in Fig. 4 at each location of the PMMA patch, showing a linear relationship between CD and g_c under RCP incidence. The highest values of CD at around 0.3 and g_c at around 0.14 are obtained when the PMMA patch covers the right corner area with large optical chirality (indicated by the red dashed box in the inset). It shows that the far-field CD response of the metasurface is linearly correlated with the dissymmetric near-field optical chirality distribution of the resonance mode.

In summary, we have demonstrated the circular dichroism response of an achiral metasurface induced by spatially selective coupling with PMMA molecules. The designed achiral metasurface with a V-shaped resonator exhibits large optical chirality with a strongly dissymmetric distribution under circularly polarized light incidence. By introducing a PMMA molecule layer on top of the metasurface, which covers the area with large optical chirality, CD in absorption of 0.38 is achieved due to the spatially selective coupling of the PMMA molecules with the metasurface. Furthermore, the difference in the optical chirality distribution of the metasurface coupled with the PMMA molecules under LCP and RCP incidences leads to the dissymmetric factor of optical chirality g_c of 0.16. In addition, the absorption spectra of the metasurface coupled with the PMMA molecules under LCP and RCP incidences are investigated with the coupled harmonic oscillator model, revealing stronger coupling strength between the PMMA layer and the metasurface under RCP incidence. Finally, it is demonstrated that the far-field CD response of the metasurface is linearly correlated with the dissymmetric near-field optical chirality distribution. It is noted that different types of achiral metasurfaces with the strong dissymmetric distribution of optical chirality and variation of the spatially selective molecular coating on metasurfaces can be further explored to increase the induced CD response. These results open further opportunities for applications in chiral molecule vibrational sensing, spatially resolved molecular detection, thermal emission control, and infrared chiral imaging.

Funding. National Science Foundation (ECCS-2230069, ECCS-2230071).

Disclosures. The authors declare no conflicts of interest.

Data availability. Data underlying the results presented in this paper are not publicly available at this time but may be obtained from the authors upon reasonable request.

REFERENCES

1. G. Serrera, J. González-Colsa, V. Giannini, *et al.*, J. Quant. Spectrosc. Radiat. Transfer **284**, 108166 (2022).
2. E. Hendry, T. Carpy, J. Johnston, *et al.*, Nat. Nanotechnol. **5**, 783 (2010).
3. S. Jeon and S. J. Kim, Appl. Sci. **11**, 2989 (2021).
4. J. Mun, M. Kim, Y. Yang, *et al.*, Light: Sci. Appl. **9**, 139 (2020).
5. C. Xu, Z. Ren, H. Zhou, *et al.*, Adv. Funct. Mater. **34**, 2314482 (2024).
6. A. Biswas, P. Cencillo-Abad, M. W. Shabbir, *et al.*, Sci. Adv. **10**, eadk2560 (2024).
7. G. Rui, S. Zou, B. Gu, *et al.*, J. Phys. Chem. C **126**, 2199 (2022).
8. E. Mohammadi, A. Tittl, K. L. Tsakmakidis, *et al.*, ACS Photonics **8**, 1754 (2021).
9. E. Mohammadi, A. Tavakoli, P. Dehkhoda, *et al.*, ACS Photonics **6**, 1939 (2019).
10. S. Zu, T. Han, M. Jiang, *et al.*, Nano Lett. **19**, 775 (2019).
11. S. Zu, T. Han, M. Jiang, *et al.*, ACS Nano **12**, 3908 (2018).
12. M. S. Mahmud, D. Rosenmann, D. A. Czaplewski, *et al.*, Opt. Express **28**, 21192 (2020).
13. H. Tang, D. Rosenmann, D. A. Czaplewski, *et al.*, Opt. Express **30**, 20063 (2022).
14. F. Cheng, X. Yang, and J. Gao, Opt. Lett. **39**, 3185 (2014).
15. M. L. Solomon, J. Hu, M. Lawrence, *et al.*, ACS Photonics **6**, 43 (2019).
16. A. García-Etxarri and J. A. Dionne, Phys. Rev. B **87**, 235409 (2013).
17. Y. Tang and A. E. Cohen, Science **332**, 333 (2011).
18. G. Duan, C. Zhang, A. Li, *et al.*, Nanoscale Res. Lett. **3**, 118 (2008).
19. W. Wan, X. Yang, and J. Gao, Opt. Lett. **24**, 12367 (2016).
20. F. Cheng, X. Yang, and J. Gao, Sci. Rep. **5**, 14327 (2015).

131.151.252.66 (a) 2025-01-08 14:01:30